Journal of Materials Chemistry A

ROYAL SOCIETY OF CHEMISTRY

COMMUNICATION

View Article Online
View Journal | View Issue

Cite this: J. Mater. Chem. A, 2023, 11, 16963

Received 7th June 2023
Accepted 20th July 2023

DOI: 10.1039/d3ta03358a

rsc.li/materials-a

$InCl_3$-modified SnO_2 as an electron transporting layer for Cd-free antimony selenide solar cells†

Lei Huang,‡[ab] Junjie Yang,‡[ab] Yujian Xia,‡[c] Peng Xiao,[ab] Huiling Cai,[ab] Aoxing Liu,[ab] Yan Wang,[ab] Xiaosong Liu,*[c] Rongfeng Tang,*[ab] Changfei Zhu[ab] and Tao Chen*[ab]

Solar cells based on Sb_2Se_3 have attracted increasing attention due to its excellent optoelectronic properties and low-cost fabrication. Up to now, high-efficiency Sb_2Se_3 solar cells with a superstrate structure have always used CdS as an electron transport layer (ETL). However, the parasitic absorption caused by CdS reduces the light absorption of the Sb_2Se_3 absorber layer, and combined with the toxicity of the Cd element, jointly causes its limitation in practical application. Tin oxide (SnO_2) is a wide-bandgap ETL and has been widely used in solar cells due to its suitable energy level, high electron mobility, and good stability. However, Sb_2Se_3 films deposited on metal oxides always exhibit poor quality. In this study, we demonstrate a facile strategy to improve the quality of an Sb_2Se_3 film by modifying a SnO_2 layer with $InCl_3$. We find that $InCl_3$ post-treatment can optimize the band alignment between SnO_2 and Sb_2Se_3, improve the quality of the SnO_2/Sb_2Se_3 heterojunction, and reduce deep-level defects. As a result, the PCE improves from 1.51% to 5.52%. Thus, this work offers a simple and effective way to improve the quality of Sb_2Se_3 films deposited on SnO_2 ETLs and provides a new path towards fabricating Cd-free Sb_2Se_3 solar cells.

Introduction

Binary antimony selenide (Sb_2Se_3), consisting of earth-abundant and low-toxicity elements, is considered as a promising light-absorbing material due to its excellent optoelectronic properties, such as an ideal optical band gap (~1.0–1.3 eV), a high light absorption coefficient (>10^5 cm^{-1} in the visible region) and decent carrier mobility (~10 cm^2 V^{-1} s^{-1}).[1] According to the Shockley–Queisser (S–Q) limit, the maximum power conversion efficiency (PCE) of an Sb_2Se_3 single-junction solar cell can reach 33.3%.[2] The narrow band gap of Sb_2Se_3 suggests that it can also be used as a bottom active layer in tandem solar cells, indicating its great potential in photovoltaic applications.[3]

Since 2013, Sb_2Se_3 solar cells have experienced rapid progress, when a solution-processed sensitized type device with a power conversion efficiency (PCE) of 3.21% was fabricated, while Tang *et al.* prepared the first planar-type Sb_2Se_3 solar cells with a PCE of 2.26% in the same year.[4,5] Since then, the focus has been mainly on planar Sb_2Se_3 solar cells including superstrate and substrate configurations, so studies in terms of the deposition of the active layer, optimization of the device structure, and the passivation of defects were conducted.[6–9] Up to now, the PCEs of Sb_2Se_3 solar cells based on superstrate and substrate configurations have both exceeded 10%, where Sb_2Se_3 films were prepared by chemical bath deposition (CBD) and closed-space sublimation (CSS) methods, respectively.[7,10] The melting point of Sb_2Se_3 is only about 608 °C, which leads to a high saturation vapor pressure below this temperature. This feature indicates that vapor deposition methods are promising routes to prepare high-quality Sb_2Se_3 films.[11] For the superstrate structure, substrates, *i.e.* electron transport layers (ETLs), play an important role in the quality of the subsequently deposited Sb_2Se_3 film.[12,13]

At present, high-efficiency Sb_2Se_3 solar cells usually use CdS as the ETL.[7,9] However, the narrow band gap of CdS (2.4 eV) usually causes parasitic absorption in the wavelength range below 520 nm, which reduces the light absorption of the Sb_2Se_3 absorber layer. This characteristic ultimately leads to a decrease in the short-circuit current density (J_{SC}) of the solar cells.[14] On the other hand, the toxicity of Cd largely limits its practical applications.[15] Thus, it is of great significance to replace CdS substrates and develop efficient Cd-free Sb_2Se_3 solar cells. In this regard, metal oxide semiconductors, including TiO_2, ZnO, SnO_2, *etc.* have been used as ETLs for Sb_2Se_3 solar cells.

[a]Hefei National Research Center for Physical Sciences at the Microscale, CAS Key Laboratory of Materials for Energy Conversion, School of Chemistry and Materials Science, University of Science and Technology of China, Hefei, Anhui 230026, China. E-mail: rftang@ustc.edu.cn; tchenmse@ustc.edu.cn

[b]Institute of Energy, Hefei Comprehensive National Science Center, Hefei, China

[c]National Synchrotron Radiation Laboratory (NSRL), University of Science and Technology of China, Hefei, Anhui 230029, China. E-mail: xsliu19@ustc.edu.cn

† Electronic supplementary information (ESI) available. See DOI: https://doi.org/10.1039/d3ta03358a

‡ These authors contributed equally to this work.

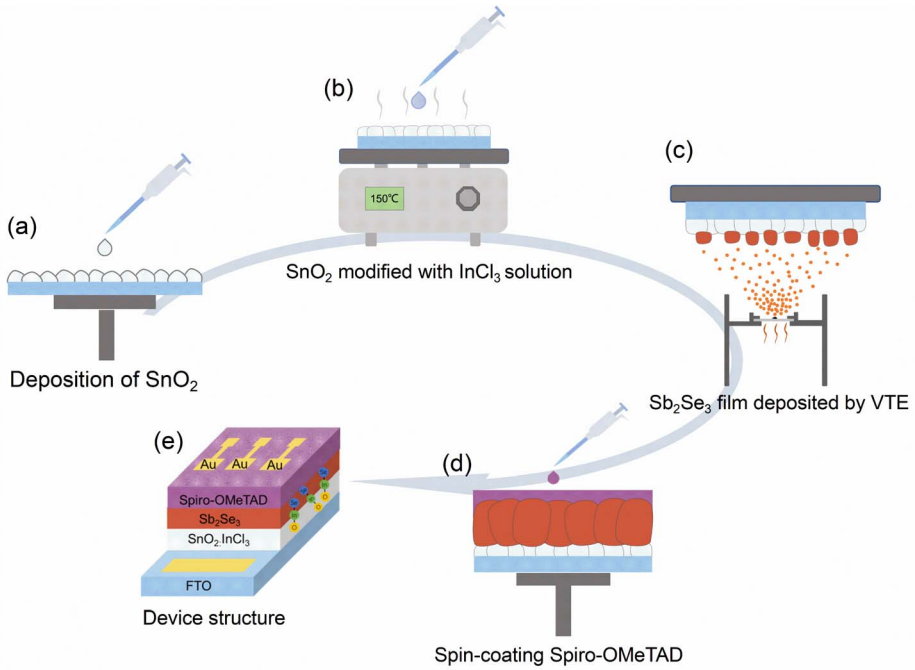

Scheme 1 The fabrication process of an Sb_2Se_3 based solar cell. (a) Deposition of SnO_2. (b) SnO_2 modified with $InCl_3$ solution. (c) Sb_2Se_3 film deposited by VTE. (d) Spin-coating Spiro-OMeTAD. (e) Device structure.

Combined with doping and interface modification strategies, the PCEs of devices based on TiO_2 and ZnO ETLs have reached 7.62% and 5.93%, respectively.[16,17] While for the wide-bandgap tin oxide (SnO_2) semiconductor, its suitable energy level, high electron mobility and good stability determine its great potential as an electron transport layer for solar cells.[18,19] Leng *et al.* demonstrated that hot electron extraction at the SnO_2/Sb_2Se_3 interface was much faster than that at the CdS/Sb_2Se_3 interface, which can successfully suppress the trapping process.[20] However, the Sb_2Se_3 film deposited on SnO_2 is not as good as that on CdS, which gives rise to a poor heterojunction interface between SnO_2 and Sb_2Se_3 layers.[21] Interface modification is an effective way to improve the quality of the heterojunction.[22–26] For instance, Wang *et al.* treated TiO_2 ETLs with $CdCl_2$, increasing the nucleation sites on the TiO_2 thin film, which improved the quality of the heterojunction.[27] In addition, Wang *et al.* passivated TiO_2 ETLs with $TiCl_4$, which could adjust the energy band arrangement of the interface and the crystal orientation of the Sb_2Se_3 film, thereby reducing interface defects and improving device performance.[28]

Inspired by the above studies, we employed SnO_2 as the ETL in Sb_2Se_3 solar cells. Here, we propose a new interface strategy of using $InCl_3$ solution to treat SnO_2, followed by a post-annealing treatment, to prepare $InCl_3$ modified SnO_2, as illustrated in Scheme 1. Subsequently, Sb_2Se_3 films were deposited through a thermal evaporation deposition. Notably, the $InCl_3$-modified SnO_2 not only significantly improved the crystallinity of Sb_2Se_3 films and increased the grain size, but also optimized the band alignment between SnO_2 and Sb_2Se_3. Furthermore, the deep-level defects in Sb_2Se_3 were reduced, and thus prolonged the carrier lifetime of the absorber layer. As a result, the efficiency of the solar cell improves to 5.52%, which is the highest PCE among completely Cd-free Sb_2Se_3 solar cells prepared by vacuum thermal evaporation.

Experimental

Preparation of SnO_2 and $InCl_3$ modified SnO_2 layers

Before the deposition of SnO_2 and the modification of SnO_2 with $InCl_3$, FTO-coated glasses should be cleaned with deionized (DI) water, isopropanol, acetone, and ethanol for 40 minutes sequentially. A UV ozone cleaner (HF-Kejing, PCE-22-LD) was employed to clean the organic residues on the surface of FTO-coated glasses. Then, the SnO_2 film was prepared by spin coating SnO_2 precursor solution at 2000 rpm for 40 s and, subsequently, a post annealing treatment at 200 °C for 30 min. In this process, the SnO_2 precursor solution was prepared by mixing a commercial SnO_2 aqueous colloidal dispersion (15 wt%, Alfa Aesar) with deionized water (1 : 1 v/v). The $InCl_3$ modified SnO_2 layer was prepared by spin-coating $InCl_3$ solution at 3000 rpm for 30 s and baking in a N_2 atmosphere at 200 °C for 30 min. In this process, the $InCl_3$ solution was obtained by dissolving 20 mg of $InCl_3 \cdot 4H_2O$ powder into 1 mL absolute alcohol and then stirring until the powder was dissolved completely.

Fabrication of Sb_2Se_3 solar cells

The Sb_2Se_3 films were deposited on FTO/SnO_2 substrates with or without $InCl_3$ treatment by vacuum thermal evaporation under a vacuum pressure of 5.0×10^{-4} Pa. The substrate temperature was controlled at 300 °C. High-purity Sb_2Se_3 powder (99.99%, Zhongnuoxincai) was used as the evaporation source and the

evaporation rate was 40–120 nm s^{-1}. Then, the as-deposited Sb_2Se_3 thin film was annealed at 300 °C for 30 min. After the post-annealing treatment, Spiro-OMeTAD was spin-coated on the surface of Sb_2Se_3 films at 3000 rpm for 30 s and baked at 100 °C for 10 min. Finally, a Au electrode was deposited using a thermal evaporator under a pressure of 5.0×10^{-4} Pa. The active area of the device was defined as 0.105 cm^2.

Chemical and morphological characterization

X-Ray diffraction (XRD) patterns were recorded using a Bruker Advance D8 diffractometer with Cu Kα radiation ($\lambda = 1.5406$ Å). The surface and cross-sectional images of SnO_2, Sb_2Se_3 thin films, and the devices were recorded using a field emission scanning electron microscope (SEM, Hitachi SU8220) equipped with an energy dispersive spectroscopy (EDS) module (Bruker). X-Ray photoelectron spectroscopy (XPS, Thermal Scientific K-Alpha+ an instrument equipped with a monochromatic Al Kα X-ray source) were used to characterize the chemical composition of SnO_2 and Sb_2Se_3. The synchrotron radiation photoemission spectroscopy (SRPES) spectra of Sn 3d and O 1s were measured at the BL11U beamline in the National Synchrotron Radiation Laboratory (NSRL) in Hefei, China. Atomic force microscope (AFM) measurement (Bruker Dimension Edge) was performed to characterize the roughness of SnO_2 and Sb_2Se_3 films. Ultraviolet-visible (UV-vis) spectroscopy (SOLID3700) was used to measure the light absorption of SnO_2 and Sb_2Se_3 thin films. Ultraviolet photo-electron spectroscopy (UPS) were measured conducted to detect the Fermi level and valence band of SnO_2 and Sb_2Se_3 using a PHI5000 VersaProbe III (Scanning ESCA Microprobe) SCA (Spherical Analyzer) and a He(I) discharge lamp (21.2 eV). Raman spectra were recorded using a Renishaw Raman spectrometer with 532 nm laser excitation. Secondary ion mass spectrometry (SIMS) was conducted to analyse the distribution of In and Cl elements at the interfaces and their diffusion into the Sb_2Se_3 film.

Optical and electrical characterization studies of the devices

Current density–voltage (J–V) curves of the Sb_2Se_3 solar cells were recorded using a standard xenon lamp solar simulator illumination with a Keithley 2400 digital Source-Meter under AM 1.5G illuminations (100 mW cm^{-2}) in ambient air at room temperature. A halogen lamp single source illumination system combined with a monochromator is used to measure the incident photon-to-current conversion efficiency (model SPIEQ200). Electrochemical impedance spectroscopy (EIS) were obtained using a Zahner Mess System PP211 electrochemical workstation at a bias potential of −0.5 V in the dark. Transient absorption spectroscopy (TAS) of the Sb_2Se_3 thin films were measured using a commercial Helios setup from Ultrafast Systems. Additionally, the pump and probe laser pulses were generated by frequency doubling the fundamental output (Coherent Vitesse, 80 MHz, Ti-sapphire laser) and through white light generated with a sapphire plate, respectively. The decay kinetics are fitted using the biexponential model $y = \sum A_i \exp(-x/\tau_i)$, and carrier lifetime ($\tau$) was obtained using equation $\tau = \sum A_i\tau_i^2/\sum A_i\tau_i$ ($i = 2$). Deep level transient spectrum (DLTS) measurement was performed *via* a Phystech FT-1230 HERA DLTS system equipped with a 10 mW red laser (laser pulse with 635 nm wavelength & pulse voltage: 0.5 V). A modified Boonton 7200 capacitance meter (1–75 kHz) was used to examine dynamic capacitance. The DLTS temperature scan range was from 120 to 420 K with 2 K heating intervals. The pulse mode was set as electrical (pulse voltage) and optical (laser excitation) double pulses, and they were exerted and removed simultaneously. In detail, the reverse bias, pulse voltage, pulse width (electric and optical), and period width were −0.4 V, 0.2–0.6 V, 10 ms, and 100 ms, respectively.

Results and discussion

Chemical and morphological characterization studies

In this work, SnO_2 films were prepared by spin-coating a diluted commercial SnO_2 aqueous colloidal dispersion, as illustrated in Scheme 1. The specific details of the preparation are presented in the Experimental section. After thermal annealing at 150 °C for 30 min, we observed that the deposited SnO_2 film on FTO-coated glasses is composed of nanoparticles (Fig. 1a) and exhibited uniform and compact morphology. After treating SnO_2 with $InCl_3$, the film becomes denser and flatter (Fig. 1b), corresponding to a decrease in root-mean-square roughness (R_q) from 19.1 nm of SnO_2 to 17.4 nm of $InCl_3$ modified SnO_2 (Fig. S1a and b†). The decrease in R_q is mainly due to the diffusion of the In element into the SnO_2 film during the annealing process, which slightly changes its surface morphology. Here, for convenience of discussion, the SnO_2 film treated with $InCl_3$ is denoted as SnO_2:$InCl_3$.

To study the surface components and chemical states of SnO_2:$InCl_3$ and SnO_2, we conducted X-ray photoelectron spectroscopy (XPS) characterization. The high-resolution XPS spectra of In 3d, Cl 2p, Sn 3d and O 1s core-level regions are displayed in Fig. 1c–f. All XPS results are corrected using the reference of C 1s (284.8 eV). Notably, in the SnO_2:$InCl_3$ film, two peaks with binding energies of 445.2 eV and 452.8 eV are detected (Fig. 1c), which correspond to In $3d_{5/2}$ and In $3d_{3/2}$, respectively. Meanwhile, we detected a signal belonging to Cl 2p (Fig. 1d). The presence of In and Cl elements is due to the $InCl_3$ post-treatment. Furthermore, the peaks at 486.4 eV and 494.8 eV can be assigned to Sn $3d_{5/2}$ and Sn $3d_{3/2}$ of the SnO_2 film (Fig. 1e), while the two peaks in the SnO_2:$InCl_3$ film shift 0.6 eV towards high binding energy. This phenomenon is mainly due to the doping of the In element into SnO_2 as an electron acceptor, which leads to the electron transfer from Sn to In, thereby increasing the binding energy of Sn. Likewise, as shown in Fig. 1f, the O 1s peak of the SnO_2:$InCl_3$ film can be divided into three peaks at 530.8 eV, 532.1 eV and 532.6 eV, corresponding to O–Sn (O_{Sn}), O–In (O_{In}) and adsorbed oxygen (O_H), respectively. Compared with pristine SnO_2, the O_{Sn} and O_H peaks in the SnO_2:$InCl_3$ film also exhibit higher binding energy due to the formation of an In–O bond. Combined with the detected In and Cl elements, we demonstrate the formation of an InO_xCl_{3-2x} phase.[29] Furthermore, we applied synchrotron radiation photoemission spectroscopy (SRPES) to measure the Sn Cl 3d and O 1s at different photon energies (Fig. 2Sa and b†). The elemental composition at different depths was detected by

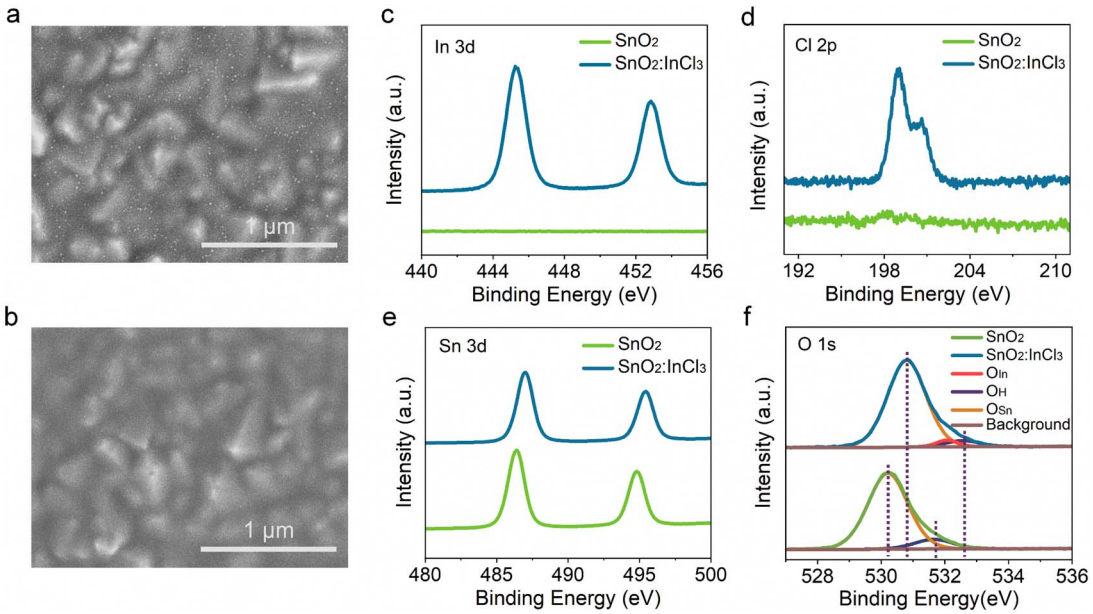

Fig. 1 Surface SEM images of (a) SnO_2 and (b) SnO_2:$InCl_3$ films. (c) High-resolution XPS spectra of (c) In 3d, (d) Cl 2p, (e) Sn 3d, and (f) O 1s elements in SnO_2 and SnO_2:$InCl_3$ films.

adjusting incident photon energies of 600, 800, 1486, and 2984 eV. With an increase in incident photon energy, that is, the detection depth deepened, the Sn 3d and O 1s peaks moved towards low binding energy, which indicates that In is mainly enriched on the surface of the SnO_2 film and gradually decreases with an increase in the depth.[30]

The transmittance spectra of FTO, FTO/SnO_2, and FTO/SnO_2:$InCl_3$ are shown in Fig. 2a. Notably, the deposited SnO_2 layer improves the transmittance of FTO glass in the wavelength range from 300 nm to 700 nm. This result is due to the decrease in surface roughness of FTO/SnO_2, reducing the light scattering and improving the flat transmittance of light.[31] After treatment with $InCl_3$, FTO/SnO_2 exhibits no significant change in transmittance compared to pristine SnO_2, which is due to the wider band gap of the formed InO_xCl_{3-2x} that avoids additional absorption. As shown in Fig. S3a and b,† the calculated bandgaps (E_g) of SnO_2 and SnO_2:$InCl_3$ are both 3.94 eV according to the Tauc plot.

$$(\alpha h\nu)^n = A(h\nu - E_g)$$

where α is the absorption coefficient; ν is the frequency of the incident photon; A is a constant; h is Planck's constant; while n equals 2 here.

In order to study the influence of $InCl_3$ treatment on the electrical properties of the SnO_2 ETL, we tested the conductivity of SnO_2 and SnO_2:$InCl_3$. Fig. 2b shows the current density–voltage (J–V) curves of the devices with structures of FTO/SnO_2/Au and FTO/SnO_2:$InCl_3$/Au. From the slopes of the curves, we obtained the conductivity (σ^0) of the films according to equation $I = \sigma^0 A d^{-1} V$, where A and d represent the area and thickness of the samples, respectively. From this, a larger slope indicates a higher conductivity. After the $InCl_3$ treatment, SnO_2:$InCl_3$

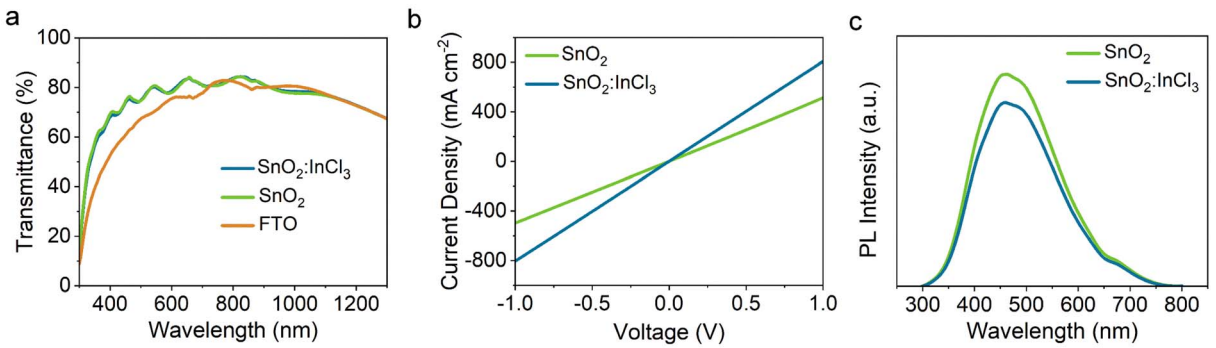

Fig. 2 (a) Transmission spectra of FTO substrates, and the FTO substrates coated with SnO_2 and SnO_2:$InCl_3$ layers. (b) Current density–voltage curves of SnO_2 and SnO_2:$InCl_3$ films. (c) PL spectra of SnO_2 and SnO_2:$InCl_3$ films.

exhibits a steeper slop than pristine SnO_2, indicating that $InCl_3$ treatment reduces the defect concentration. The corresponding $J^{1/2}$–V curves are presented in Fig. S4† and the carrier mobilities are calculated using the Mott–Gurney formula $J = 9/8\varepsilon_0\varepsilon_r\mu V^2/\hat{d}^3$, where J, ε_0, ε_r, μ, V, and d represent the current density, the vacuum dielectric constant, the relative dielectric constant of the electron transport layer, the electron mobility, the voltage, and the film thickness, respectively. Accordingly, the carrier mobilities of SnO_2 and SnO_2:$InCl_3$ were calculated to be 2.96×10^{-4} $cm^2\ V^{-1}\ s^{-1}$ and 1.88×10^{-4} $cm^2\ V^{-1}\ s^{-1}$, respectively. The increase in conductivity and carrier mobility can be attributed to the passivation of deep-level defects in SnO_2 films, which is beneficial for improving charge transfer at the interface of Sb_2Se_3/ETLs. Subsequently, steady-state photoluminescence (PL) spectroscopy was conducted to demonstrate the changes in defects in SnO_2 films before and after $InCl_3$ treatment. As shown in Fig. 2c, the SnO_2 film treated with $InCl_3$ shows a weakened PL signal. Since the PL intensity is proportional to the defect concentration, the decreased intensity indicates that $InCl_3$ treatment reduces the defect concentration as well as the carrier recombination in SnO_2 ETLs.[32]

In superstrate solar cells, an ETL is not only used for transporting electrons, but also has a significant impact on the quality of the subsequent deposited absorber layer. To investigate the influence of substrates on the absorber layer of Sb_2Se_3, we deposited Sb_2Se_3 films on SnO_2 and SnO_2:$InCl_3$ by thermal evaporation. For convenience, the Sb_2Se_3 films deposited on SnO_2 and SnO_2:$InCl_3$ are denoted as SnO_2/Sb_2Se_3 and SnO_2:$InCl_3$/Sb_2Se_3, respectively. The XRD patterns of the two samples are shown in Fig. 3e. Except for the peaks from the FTO substrate, all peaks can be indexed to orthorhombic Sb_2Se_3 (JCPDS no. 15-0681). In the Raman spectrum (Fig. S5†), both films exhibit three dominant peaks corresponding to the Sb_2Se_3 phase at 151, 189, and 209 cm^{-1}. Based on the above results, we confirm that the Sb_2Se_3 films deposited by VTE have high purity.

Furthermore, the treatment of SnO_2 ETLs significantly changed the morphology of Sb_2Se_3 films, as shown in the SEM images in Fig. 3a–c. The $InCl_3$-modified SnO_2 increases the average grain size of Sb_2Se_3 from about 200 nm to 500 nm (Fig. 3f and S6†), which can reduce the recombination loss at grain boundaries (GBs). Moreover, compared with the Sb_2Se_3 film on SnO_2, the surface morphology of the Sb_2Se_3 film deposited on SnO_2:$InCl_3$ is flatter, with R_q decreasing from 26.6 to 20.8 nm (Fig. 3b–d), which is favourable to improving the contact between the absorber layer and hole transport layer, thereby reducing the leakage current of the solar cell.

To probe the impact of $InCl_3$ post-treatment on the energy level alignment between SnO_2 and Sb_2Se_3, ultraviolet photoelectron spectroscopy (UPS) was used to measure the valence band maximum (VBM) and Fermi level (E_F). As shown in Fig. 4a–d, the E_F of SnO_2 and SnO_2:$InCl_3$ are measured to be −3.95 and −4.28 eV, respectively. By linear extrapolation of the low binding energy region, the gaps (E_P) between the Fermi level and valence band maximum are estimated to be 3.55 and 3.38 eV for SnO_2 and SnO_2:$InCl_3$, respectively. Combined with the same optical band gap of 3.94 eV (Fig. S3†), the conduction band minimum (CBM) corresponding to SnO_2 and SnO_2:$InCl_3$

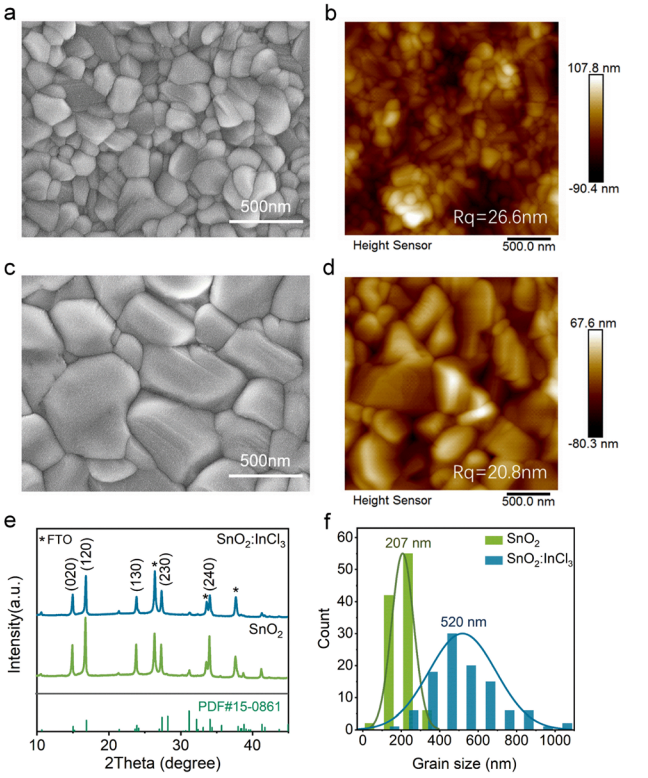

Fig. 3 Surface SEM images of Sb_2Se_3 films on (a) SnO_2 and (c) SnO_2:$InCl_3$ layers. AFM images of Sb_2Se_3 films on (b) SnO_2 and (d) SnO_2:$InCl_3$. (e) XRD patterns of the Sb_2Se_3 films that were deposited on SnO_2 and SnO_2:$InCl_3$ films, with FTO as the substrate. (f) Statistical distribution of the grain size in Sb_2Se_3 films on SnO_2 and SnO_2:$InCl_3$ films.

is calculated to be −3.56 eV and −3.72 eV, respectively. Similarly, the E_g, E_F, E_P and CBM of Sb_2Se_3 deposited on the SnO_2 and SnO_2:$InCl_3$ substrates are measured to be 1.25 eV, −4.70 eV, 0.47 eV, and −3.97 eV and 1.25 eV, −4.54 eV, 0.51 eV, and −3.85 eV, respectively (Fig. 4b–d).[22] The schematic diagrams of energy level alignment between the ETL and Sb_2Se_3 films are shown in Fig. 4e and f. Consequently, the conduction band offset (CBO) of SnO_2/Sb_2Se_3 and SnO_2:$InCl_3$/Sb_2Se_3 heterojunctions is calculated to be −0.41 eV ($-\Delta E_C$) and −0.13 eV ($-\Delta E_C$), respectively. Notably, both interfaces have "spike" like energy level alignment, while a mild spike ($0.1 \leq \Delta E_C \leq 0.2$ eV) is believed to reduce the carrier recombination.[33] Therefore, the improved band alignment between SnO_2:$InCl_3$ and Sb_2Se_3 can facilitate efficient carrier transport in a solar cell and is expected to improve the device efficiency.

After interface treatment of SnO_2, the quality of subsequently deposited Sb_2Se_3 films was significantly improved. In order to gain insight into the improvement mechanism of the film quality, we utilized secondary ion mass spectrometry (SIMS) to detect the vertical distribution of elements in ETLs/Sb_2Se_3. As shown in Fig. 5a, we observe severe diffusion of Se into the SnO_2 layer in the absence of $InCl_3$ treatment, which may lead to the formation of $SnO_{2-x}Se_x$, resulting in a poor heterojunction.[16] In contrast, $InCl_3$ treatment hinders the diffusion of the Se

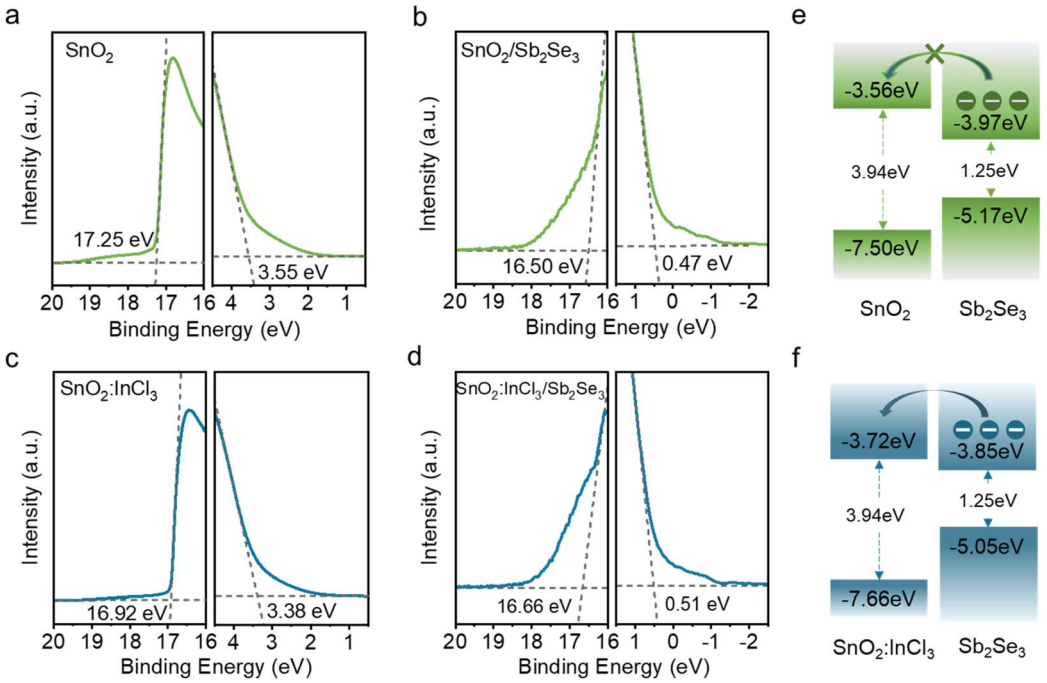

Fig. 4 The UPS spectra of (a) SnO_2, (b) SnO_2/Sb_2Se_3, (c) SnO_2:$InCl_3$, and (d) SnO_2:$InCl_3/Sb_2Se_3$. A diagram of the energy band alignments at the interfaces between Sb_2Se_3 and (e) SnO_2 and (f) SnO_2:$InCl_3$.

element into SnO_2, while allowing the Cl element to diffuse into Sb_2Se_3, which is beneficial for passivating defects in the absorption layer, as demonstrated in previous studies (Fig. 5d).[34] Afterwards, we analyzed the bonding information at the interface through XPS. When 3 nm of the Sb_2Se_3 film was deposited on the SnO_2:$InCl_3$ substrate, we detected the presence of the In element in Sb_2Se_3 (Fig.S7†). In specific, the In 3d peak can be divided into three kinds of peaks. The peaks at 444.5 eV

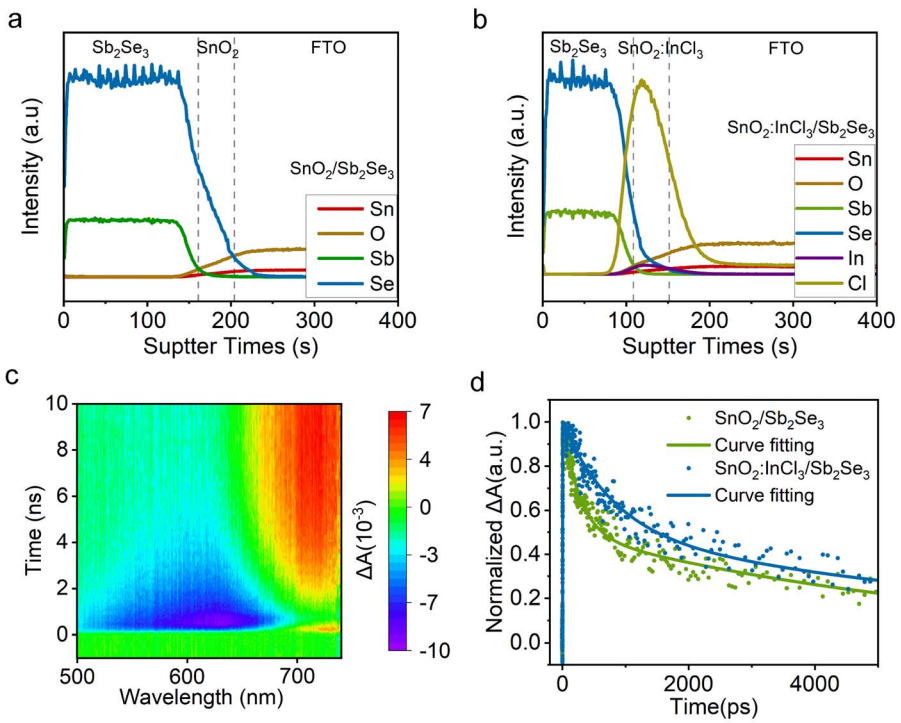

Fig. 5 The secondary ion mass spectroscopy (SIMS) spectra of (a) SnO_2/Sb_2Se_3 and (b) SnO_2:$InCl_3/Sb_2Se_3$. (c) TAS mapping of SnO_2:$InCl_3$/Sb_2Se_3. (d) Transient decay kinetics (scatter) and fit (solid lines) monitored at 690 nm for Sb_2Se_3 films deposited on SnO_2 and SnO_2:$InCl_3$.

and 451.9 eV, 445.2 eV and 452.7 eV, and 446.0 eV and 453.5 eV can be assigned to In^{3+} that bonded with Se^{2-}, O^{2-} and Cl^{-}, respectively. The formed In–Se and In–O bonds indicate that In serves as a bridge between SnO_2 and Sb_2Se_3, which can improve the carrier extraction and transport at the interface.[22] Thus, transient absorption spectroscopy (TAS) was performed to compare the kinetics of carrier transport at the interface of ETLs/Sb_2Se_3. In this measurement, a 360 nm pump pulse laser is selected as the source to excite the ground-state charge carrier in the Sb_2Se_3 films, and TAS spectra are obtained (Fig. 5c and S8†). Then, transition dynamics of the samples are extracted from the TAS spectrum near 690 nm wavelength and well fitted according to the double exponential decay equation, as shown in Fig. 5d. The fitted average lifetime of FTO/SnO_2/Sb_2Se_3 and FTO/SnO_2:$InCl_3$/Sb_2Se_3 is 5.960 and 7.877 ns, respectively. Compared with FTO/SnO_2/Sb_2Se_3, FTO/SnO_2:$InCl_3$/Sb_2Se_3 exhibits a prolonged carrier lifetime. This may be attributed to the modification of the SnO_2 ETL with $InCl_3$ improving the quality of Sb_2Se_3, thereby reducing the existing defects in the film.

To explore the deep-level defects in the films, we conducted the deep-level transient spectroscopy (DLTS) measurement. The number of defects was identified from the DLTS signal using the Fourier deconvolution algorithm, and the corresponding trap density was calculated (the characterization details are provided in Note 1 in the ESI†). The Sb_2Se_3 films deposited by the vacuum thermal evaporation method in this work display p-type conductivity. Thus, the positive and negative peaks in the DLTS spectra represent hole traps (acceptor defects) and electron traps (donor defects), respectively. As shown in Fig. 6a, both samples are detected to have two dominant deep-level acceptor defects. The detailed defect parameters including the trap energy level (E_T), capture cross section (σ), trap density (N_T), and carrier density (N_S) extracted from the DLTS spectra are summarized in Table 1. Notably, the activation energies of the trap defects in the two devices are similar, indicating that the origins of these defects are the same due to the same synthesis method. Accordingly, these two kinds of defects in the devices can be denoted as H1 and H2. Combined with the calculation results, the traps H1 and H2 located at about 0.55 and 0.66 eV above the VBM (Fig. 6c and d) can be assigned to the antimony vacancy (V_{Sb}) and selenium substitutes for antimony anti-site defects (Se_{Sb}), respectively. Both acceptor defects act as hole traps or recombination sites, which can hinder the charge transport and shorten the carrier lifetime. After the modification of SnO_2 with $InCl_3$, the trap state densities in the absorb layer are reduced compared with the control sample. The reduced defect density demonstrates that SRH recombination in the SnO_2:$InCl_3$ based device is effectively suppressed.

In order to explore the effect of $InCl_3$-modified SnO_2 on device performance, solar cells with the structure of FTO/SnO_2 (or SnO_2:$InCl_3$)/Sb_2Se_3/Spiro-OMeTAD/Au were fabricated. The corresponding cross sectional SEM image of the device is shown in Fig. S9.† Current density–voltage (J–V) curves of the devices based on SnO_2 and SnO_2:$InCl_3$ ETLs were measured under one solar illumination (100 mW cm^{-2}). The J–V curves of the best devices are shown in Fig. 7a, and the detailed parameters are listed in Table 2. Notably, the SnO_2-based device delivers an open circuit voltage (V_{OC}), a short-circuit current density (J_{SC}), a fill factor (FF), and a power conversion efficiency (PCE) of

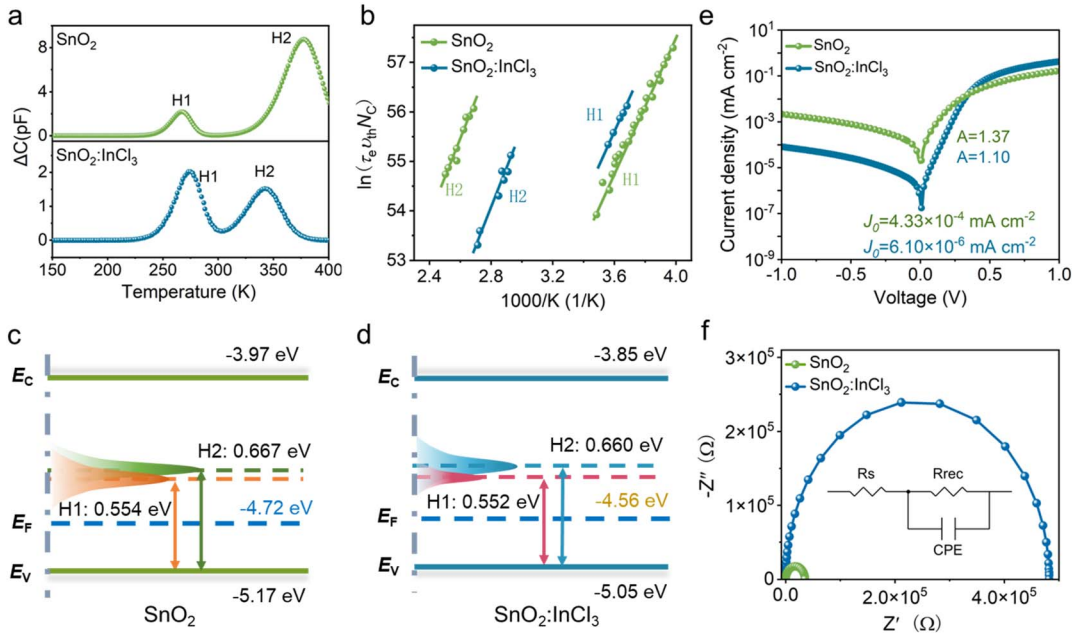

Fig. 6 Dual-pulse mode DLTS signals at variable pulse voltage (0.2–0.6 V) for (a) SnO_2/Sb_2Se_3 and (b) SnO_2:$InCl_3$/Sb_2Se_3 devices. Schematic diagram of the energy band and defect level of (c) Sb–SnO_2/Sb_2Se_3 and (d) SnO_2:$InCl_3$/Sb_2Se_3 devices. E_C, E_V, and E_F stand for the CBM, Fermi level and VBM, respectively. (e) Dark J–V curves of SnO_2/Sb_2Se_3 and SnO_2:$InCl_3$/Sb_2Se_3 devices. (f) Nyquist plots (under dark conditions at 0.50 V) of SnO_2/Sb_2Se_3 and SnO_2:$InCl_3$/Sb_2Se_3 devices.

Table 1 The trap parameters, including E_T, σ, N_T, and N_S, extracted from DLTS of the SnO_2/Sb_2Se_3 and SnO_2:$InCl_3/Sb_2Se_3$ based devices

Devices	Trap	Defect	E_T (eV)	σ (cm^2)	N_T (cm^{-3})	N_S (cm^{-3})
SnO_2/Sb_2Se_3	H1	V_{Sb}	E_V + 0.554	1.71×10^{-14}	5.42×10^{14}	4.74×10^{16}
	H2	Se_{Sb}	E_V + 0.667	4.53×10^{-16}	6.53×10^{14}	
SnO_2:$InCl_3/Sb_2Se_3$	H1	V_{Sb}	E_V + 0.552	7.37×10^{-15}	3.81×10^{14}	4.56×10^{16}
	H2	Se_{Sb}	E_V + 0.660	6.94×10^{-15}	5.87×10^{13}	

0.243 V, 15.20 mA cm^{-2}, 40.72%, and 1.51%, respectively. In comparison, the SnO_2:$InCl_3$-based device delivers enhanced photovoltaic parameters, corresponding to a V_{OC} of 0.367 V, J_{SC} of 26.44 mA cm^{-2}, FF of 56.95%, and PCE of 5.52%. The box statistical distribution of photovoltaic parameters for the two types of devices is shown in Fig. 7c–f, which further demonstrates that using $InCl_3$ to treat an SnO_2 ETL can improve the V_{OC}, J_{SC}, FF, as well as PCE of Sb_2Se_3 devices. To understand the increase in J_{SC}, we recorded the external quantum efficiency (EQE) spectrum of the devices (Fig. 7b). Compared with the SnO_2-based device, the SnO_2:$InCl_3$-based Sb_2Se_3 device exhibits a higher photo-response in the wavelength range from 350 to 1050 nm, which leads to an increase in the integrated current density from 14.41 to 25.57 mA cm^{-2}.

Dark J–V curves were tested to investigate the reverse saturation current (J_0) and diode ideal factor (n) of the solar cells (Fig. 6e). For the SnO_2:$InCl_3$-based device, the J_0 and n are estimated to be 6.10 $\times$ 10^{-6} mA cm^{-2} and 1.37, respectively, while for the SnO_2-based device, J_0 and n are 4.33 $\times$ 10^{-4} mA cm^{-2} and 1.10, respectively. Notably, n reflects the defect-assisted Shockley–Read–Hall (SRH) recombination properties of the film. Thus, the decreased n value indicates that Shockley–Read–Hall (SRH) recombination is effectively suppressed in the SnO_2:$InCl_3$ device due to the improvement of the interfacial contact and the reduced point defects in the Sb_2Se_3 film. In addition, J_0 is also significantly reduced after SnO_2 is treated with $InCl_3$. According to the following equation:

$$V_{OC} = \frac{Ak_BT}{q}\ln\left(\frac{J_{SC}}{J_0} + 1\right),$$

Table 2 Photovoltaic parameters of the optimal devices based on SnO_2/Sb_2Se_3 and SnO_2:$InCl_3/Sb_2Se_3$

Devices	V_{OC} (V)	J_{SC} (mA cm^{-2})	FF (%)	PCE (%)
SnO_2/Sb_2Se_3	0.243	15.20	40.72	1.51
SnO_2:$InCl_3/Sb_2Se_3$	0.367	26.44	56.95	5.52

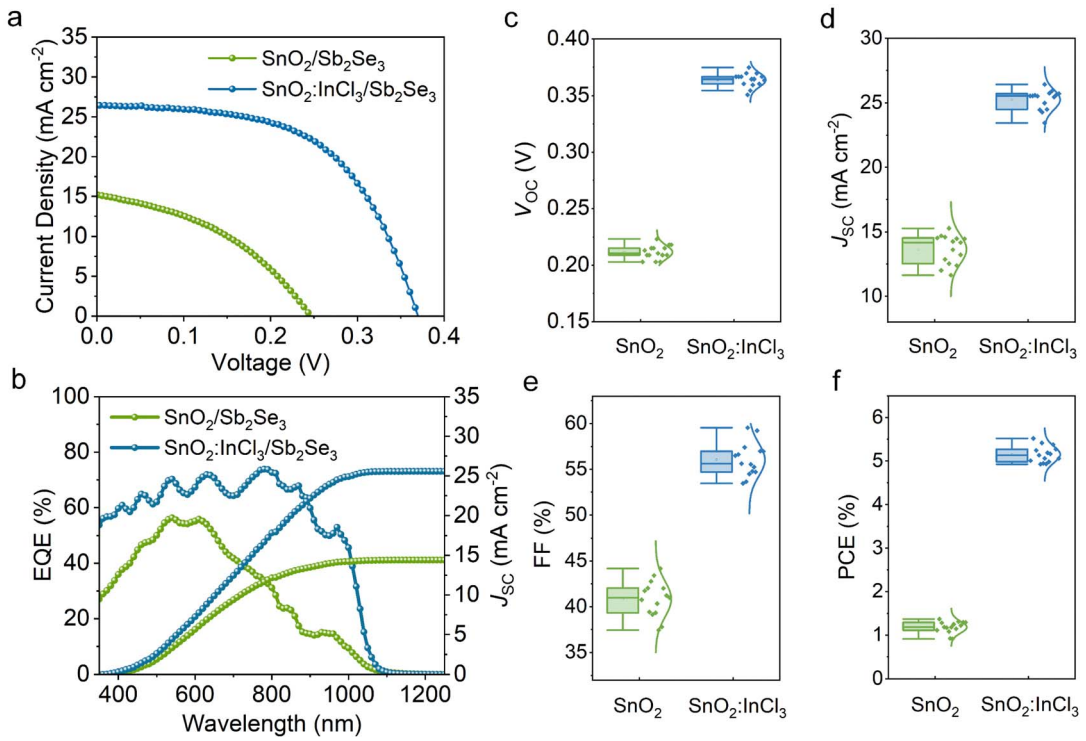

Fig. 7 a) Current density–voltage (J–V) characteristics and (b) external quantum efficiency (EQE) spectra of the optimal SnO_2/Sb_2Se_3 and SnO_2:$InCl_3/Sb_2Se_3$ devices. Statistical boxplots of (c) conversion efficiency (%), (d) V_{OC} (V), (e) fill factors (%), and (f) J_{SC} (mA cm^{-2}) for SnO_2/Sb_2Se_3 and SnO_2:$InCl_3/Sb_2Se_3$ solar cells.

where k_B, T, and q are the Boltzmann constant, temperature, and electron charge, respectively, the smaller J_0 indicates that the leakage current of the device is suppressed. Thus, the corresponding device exhibits a higher V_{OC}.

We further apply EIS to characterize the interfacial charge transfer in the device. Nyquist plots and a fitting equivalent electronic circuit of the solar cells are presented in Fig. 6f, where R_S and R_{REC} correspond to series resistance and recombination resistance of the device, respectively. The device with $InCl_3$ treatment exhibits a larger R_{REC} of 57.84 kΩ cm^2 and smaller R_S of 12.83 Ω cm^2 when compared with the SnO_2-based device, which correspond to a R_{REC} of 42.09 kΩ cm^2 and R_S of 22.57 Ω cm^2. The increased R_{REC} and decreased R_S indicate that the carrier recombination in the device is effectively inhibited by using $InCl_3$ to modify the SnO_2 ETL. This result is mainly attributed to the effective passivation of defects and the improved interfacial heterojunction, thus significantly improving the efficiency of the Sb_2Se_3 based solar cells.

Conclusions

In summary, we demonstrated an $InCl_3$ modified SnO_2 film and its application as an ETL in Sb_2Se_3 solar cells. $InCl_3$ post-treatment not only effectively prevents the diffusion of Se, but also guides the subsequent growth of Sb_2Se_3. The improvement of the quality of the Sb_2Se_3 film and the SnO_2/Sb_2Se_3 heterojunction resulted in a device efficiency of 5.52% for Sb_2Se_3 solar cells, which is currently the highest efficiency among Sb_2Se_3 solar cells based on SnO_2 electron transport layers. Thus, this work offers a simple and effective method for improving the quality of Sb_2Se_3 films deposited on metal oxide substrates and provides a new path towards fabricating Cd-free Sb_2Se_3 solar cells.

Author contributions

T. C., R. F. T. and L. H. conceived and designed the study. L. H. provided samples for the study. J. J. Y. performed the DLTS experiment and analysed the data. P. X. performed the TAS experiment and analysed the data. A. X. L. performed the XRD experiments. R. F. T. and Y. W. performed the XPS experiments and analysed the data. Y. J. X. performed the SRPES experiments and analysed the data. H. L. C. provided the method for preparing SnO_2 films. T. C., C. F. Z., R. F. T. and H. L. interpreted the data. T. C., R. F. T. and X. S. L. revised the manuscript. All authors contributed to the general discussion.

Conflicts of interest

The authors declare no conflict of interest.

Acknowledgements

This work was supported by the National Key Research and Development Program of China (2019YFA0405600), National Natural Science Foundation of China (22005293, U19A2092 and 22275180), Institute of Energy, Hefei Comprehensive National Science Center (Grant No. 21KZS212), and Collaborative Innovation Program of Hefei Science Center, CAS.

Notes and references

1 R. Tang, X. Wang, W. Lian, J. Huang, Q. Wei, M. Huang, Y. Yin, C. Jiang, S. Yang, G. Xing, S. Chen, C. Zhu, X. Hao, M. A. Green and T. Chen, *Nat. Energy*, 2020, **5**, 587–595.
2 A. Polman, M. Knight, E. C. Garnett, B. Ehrler and W. C. Sinke, *Science*, 2016, **352**, aad4424.
3 J. Zhang, W. Lian, Y. Yin, X. Wang, R. Tang, C. Qian, X. Hao, C. Zhu and T. Chen, *Sol. RRL*, 2020, **4**, 2000048.
4 Y. C. Choi, T. N. Mandal, W. S. Yang, Y. H. Lee, S. H. Im, J. H. Noh and S. I. Seok, *Angew. Chem.*, 2014, **53**, 1329–1333.
5 Y. Zhou, M. Leng, Z. Xia, J. Zhong, H. Song, X. Liu, B. Yang, J. Zhang, J. Chen, K. Zhou, J. Han, Y. Cheng and J. Tang, *Adv. Energy Mater.*, 2014, **4**, 1301846.
6 X. Liang, Y. Feng, W. Dang, H. Huang, X. Wang, Y. Guo, K. Shen, R. E. I. Schropp, Z. Li and Y. Mai, *ACS Energy Lett.*, 2022, **8**, 213–221.
7 Z. Duan, X. Liang, Y. Feng, H. Ma, B. Liang, Y. Wang, S. Luo, S. Wang, R. E. I. Schropp, Y. Mai and Z. Li, *Adv. Mater.*, 2022, **34**, e2202969.
8 G. Liang, Y. Luo, S. Chen, R. Tang, Z. Zheng, X. Li, X. Liu, Y. Liu, Y. Li, X. Chen, Z. Su, X. Zhang, H. Ma and P. Fan, *Nano energy*, 2020, **73**, 104806.
9 C. Jiang, R. Tang, C. Zhu and T. Chen, *J. Univ. Sci. Technol.*, 2020, **50**, 1383.
10 Y. Zhao, S. Wang, C. Li, B. Che, X. Chen, H. Chen, R. Tang, X. Wang, G. Chen, T. Wang, J. Gong, T. Chen, X. Xiao and J. Li, *Energy Environ. Sci.*, 2022, **15**, 5118–5128.
11 Y. Yin, C. Jiang, Y. Ma, R. Tang, X. Wang, L. Zhang, Z. Li, C. Zhu and T. Chen, *Adv. Mater.*, 2021, **33**, e2006689.
12 Y. Zhou, L. Wang, S. Chen, S. Qin, X. Liu, J. Chen, D.-J. Xue, M. Luo, Y. Cao, Y. Cheng, E. H. Sargent and J. Tang, *Nat. Photonics*, 2015, **9**, 409–415.
13 X. Jin, Y. Fang, T. Salim, M. Feng, Z. Yuan, S. Hadke, T. C. Sum and L. H. Wong, *Adv. Mater.*, 2021, **33**, e2104346.
14 C. Liu, S. Wu, Y. Gao, Y. Feng, X. Wang, Y. Xie, J. Zheng, H. Zhu, Z. Li, R. E. I. Schropp, K. Shen and Y. Mai, *Adv. Funct. Mater.*, 2022, **32**, 2209601.
15 Y. Zhao, C. Li, J. Niu, Z. Zhi, G. Chen, J. Gong, J. Li and X. Xiao, *J. Mater. Chem. A*, 2021, **9**, 12644–12651.
16 L. Wang, D.-B. Li, K. Li, C. Chen, H.-X. Deng, L. Gao, Y. Zhao, F. Jiang, L. Li, F. Huang, Y. He, H. Song, G. Niu and J. Tang, *Nat. Energy*, 2017, **2**, 1903914.
17 K. Li, C. Chen, S. Lu, C. Wang, S. Wang, Y. Lu and J. Tang, *Adv. Mater.*, 2019, **31**, 1903914.
18 L. Xiong, Y. Guo, J. Wen, H. Liu, G. Yang, P. Qin and G. Fang, *Adv. Funct. Mater.*, 2018, **28**, 1802757.
19 J. Tao, X. Hu, Y. Guo, J. Hong, K. Li, J. Jiang, S. Chen, C. Jing, F. Yue, P. Yang, C. Zhang, Z. Wu, J. Tang and J. Chu, *Nano Energy*, 2019, **60**, 802–809.
20 Z. Zhang, M. Hu, T. Jia, J. Du, C. Chen, C. Wang, Z. Liu, T. Shi, J. Tang and Y. Leng, *ACS Energy Lett.*, 2021, **6**, 1740–1748.

21 W. Wang, L. Yao, J. Dong, L. Wu, Z. Cao, L. Hui, G. Chen, J. Luo and Y. Zhang, *Adv. Mater. Interfaces*, 2022, **9**, 2102464.
22 X. Meng, X. Cui, M. Rager, S. Zhang, Z. Wang, J. Yu, Y. Harn, Z. Kang, B. Wagner, Y. Liu, C. Yu, J. Qiu and Z. Lin, *Nano Energy*, 2018, **52**, 123–133.
23 Y. Ma, X. Meng, K. Li, L. Zhang, Y. Du, X. Cai and J. Qiu, *ACS Catal.*, 2023, **13**, 1290–1298.
24 X. Meng, C. Yu, X. Song, J. Iocozzia, J. Hong, M. Rager, H. Jin, S. Wang, L. Huang, J. Qiu and Z. Lin, *Angew. Chem., Int. Ed.*, 2018, **57**, 4682–4686.
25 S. Bi, X. Leng, Y. Li, Z. Zheng, X. Zhang, Y. Zhang and H. Zhou, *Adv. Mater.*, 2019, **31**, 1805708.
26 Z. Gao, Y. Wang and W. Choy, *Adv. Energy Mater.*, 2022, **12**, 2104030.
27 Y. Wang, R. Tang, L. Huang, C. Qian, W. Lian, C. Zhu and T. Chen, *ACS Appl. Mater. Interfaces*, 2022, **14**, 33181–33190.
28 W. Wang, Z. Cao, H. Wang, J. Luo and Y. Zhang, *J. Mater. Chem. A*, 2021, **9**, 26963–26975.
29 X. Guo, J. Du, Z. Lin, J. Su, L. Feng, J. Zhang, Y. Hao and J. Chang, *Chem. Eng. J.*, 2021, **407**, 127997.
30 J. Ge, D. He, W. Chen, H. Ju, H. Zhang, T. Chao, X. Wang, R. You, Y. Lin, Y. Wang, J. Zhu, H. Li, B. Xiao, W. Huang, Y. Wu, X. Hong and Y. Li, *J. Am. Chem. Soc.*, 2016, **138**, 13850–13853.
31 Y. Zhao, J. Duan, H. Yuan, Y. Wang, X. Yang, B. He and Q. Tang, *Sol. RRL*, 2019, **3**, 1800284.
32 C. Chen, Y. Zhao, S. Lu, K. Li, Y. Li, B. Yang, W. Chen, L. Wang, D. Li, H. Deng, F. Yi and J. Tang, *Adv. Energy Mater.*, 2017, **7**, 1700866.
33 H. Shiel, O. S. Hutter, L. J. Phillips, J. E. N. Swallow, L. A. H. Jones, T. J. Featherstone, M. J. Smiles, P. K. Thakur, T.-L. Lee, V. R. Dhanak, J. D. Major and T. D. Veal, *ACS Appl. Energy Mater.*, 2020, **3**, 11617–11626.
34 S. Chen, M. Li, Y. Zhu, X. Cai, F. Xiao, T. Ma, J. Yang, G. Shen, A. Ke, Y. Lu, W. Liang, H. Hsu, C. Chen, J. Tang and H. Song, *Adv. Energy Mater.*, 2022, **12**, 2202897.